

Synergy of multiviewing spectroscopic diagnostics on COMPASS-D (invited)

P. G. Carolan, N. J. Conway, A. R. Field, P. B. Jones, and H. F. Meyer

Citation: *Rev. Sci. Instrum.* **72**, 881 (2001); doi: 10.1063/1.1323244

View online: <http://dx.doi.org/10.1063/1.1323244>

View Table of Contents: <http://rsi.aip.org/resource/1/RSINAK/v72/i1>

Published by the [American Institute of Physics](#).

Related Articles

Development of multi-channel Doppler spectroscopic measurement system using 8×8 multianode photomultiplier tube assembly
Rev. Sci. Instrum. **83**, 083103 (2012)

Electron density and temperature profile diagnostics for C-2 field reversed configuration plasmas
Rev. Sci. Instrum. **83**, 10E339 (2012)

Analysis of edge density fluctuation measured by trial KSTAR beam emission spectroscopy system
Rev. Sci. Instrum. **83**, 10D531 (2012)

Upgrade of the infrared camera diagnostics for the JET ITER-like wall divertor
Rev. Sci. Instrum. **83**, 10D530 (2012)

Generation and diagnostics of atmospheric pressure CO₂ plasma by laser driven plasma wind tunnel
J. Appl. Phys. **112**, 033301 (2012)

Additional information on *Rev. Sci. Instrum.*

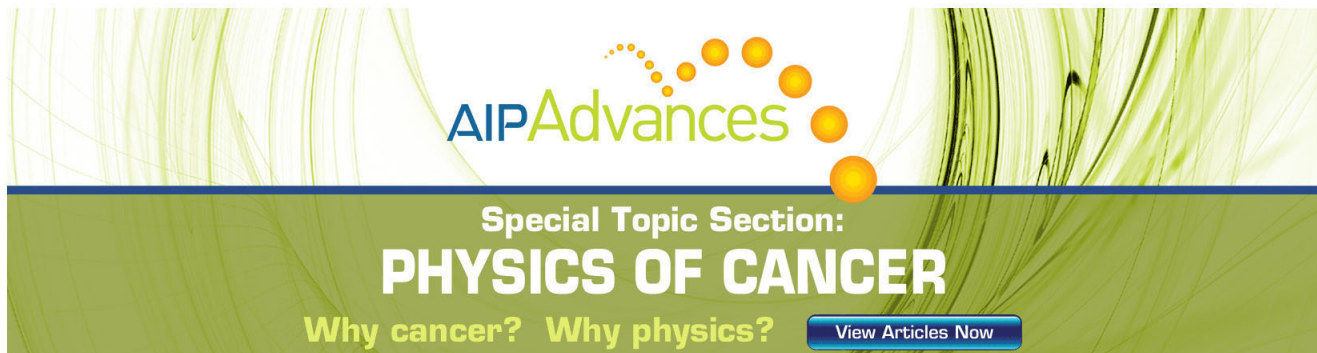
Journal Homepage: <http://rsi.aip.org>

Journal Information: http://rsi.aip.org/about/about_the_journal

Top downloads: http://rsi.aip.org/features/most_downloaded

Information for Authors: <http://rsi.aip.org/authors>

ADVERTISEMENT



AIP Advances

Special Topic Section:
PHYSICS OF CANCER

Why cancer? Why physics? [View Articles Now](#)

Synergy of multiviewing spectroscopic diagnostics on COMPASS-D (invited)

P. G. Carolan, N. J. Conway, A. R. Field, P. B. Jones,^{a)} and H. F. Meyer
*EURATOM/UKAEA Fusion Association, Culham Science Centre, Abingdon, Oxfordshire OX14 3DB,
 United Kingdom*

(Presented on 21 June 2000)

In the COMPASS-D tokamak three multiviewing diagnostic systems are combined by using the same collection optics. HeI line ratios from a helium thermal jet provide detailed edge $T_e(r)$ and $n_e(r)$ profiles. The spectrometer also provides the D_α profile. A Doppler spectrometer system provides T_i and V_θ profiles using HeII emission. The T_e and n_e profiles are used in extracting neutral densities from the D_α emissivities, and the radial electric field from the Doppler measurements. The behavior of $T_e(r)$, $n_e(r)$, $2n_D(r)$, E_r , and V_θ and their gradients can now be compared in detail to investigate the H-mode transition physics. © 2001 American Institute of Physics.

[DOI: 10.1063/1.1323244]

I. INTRODUCTION

The edge plasma region in tokamaks often exhibits rapidly varying parameters, in both the temporal and spatial domains. In particular, the phenomena accompanying H-modes, including steepening of gradients in density, temperature, and electric fields, can severely tax diagnostic techniques as the regions of interest may extend over only a few cm and changes occur within times as short as tens of microseconds (e.g., Ref. 1). Some of the phenomena are almost certainly behaving symbiotically but others will be merely symptomatic, emphasizing the importance of establishing causality in trying to clarify the underlying physics. For example, improving edge confinement may reduce the outflux of particles and consequently reduce the influx of neutrals and impurities from edge materials. Measuring profiles of the relevant quantities at different positions, or separately, may be of only limited value due to the difficulties of accurate mapping from one location to another and the inevitable non-uniformity at the cm scale in, for example, the toroidal direction. So it is not only the physics effects that can be interwoven; so also may the data interpretation from one system to another. This may be achieved if care is taken early in the design to perform the measurements at almost precisely the same place even where essentially different techniques are combined.

In recent experiments on COMPASS-D tokamak (major radius $R=0.557$ m, limiter minor radius, $a=0.22$ m) we have implemented this approach using a novel combined diagnostic consisting of a thermal helium beam diagnostic (HELIOS)² and a Doppler spectrometer (CELESTE)³ with near-identical lines of sight at the plasma boundary. The former diagnostic provides T_e and n_e profiles as well as D_α intensities.

The availability of the T_e and n_e profiles allows the evolving neutral density profile to be determined from the spatially unfolded D_α emissivity. Whereas the Doppler spec-

trometer gives direct information on impurity ion temperature and velocity profiles, the measured T_e and n_e profiles can be used to determine the emission-line excitation rates required for obtaining the ion diamagnetic drift velocity. Armed with this, the $E \times B$ drift velocity is obtained from the measured velocities yielding the radial electric field profile, $E_r(r,t)$ from a simple radial force balance consideration, i.e., $en_i Z_i (E + v_i \times B) = \nabla p_i$ for the i th ion species.

We describe the apparatus and how the data are unfolded in terms of local values and then interpreted using various codes, primarily atomic physics. The analyses are taken a stage further in mapping to, when appropriate, a flux coordinate system whose parameters are determined dynamically from magnetics using the EFIT code. This is important as most of the quantities are flux-surface invariants and we observe rapid changes in the edge flux-surface positions when journeying in and out of H-modes.

We illustrate the efficacy of combining the diagnostics in examples from H-mode campaigns on the COMPASS-D tokamak.

II. APPARATUS

COMPASS-D is the smallest tokamak ($R=0.56$ m, $a \sim 0.2$ m) with elongated ($\kappa=1.6$) single-null plasmas achieving clear H-modes and thus providing valuable contributions both to understanding the underlying physics and to scaling laws, e.g., threshold powers for achieving H-mode transitions. It can achieve H-mode with ohmic heating alone or assisted with ECRH. The plasma can be operated close to critical conditions for attaining H-mode so allowing perturbation experiments for investigating H-mode physics such as edge ECRH heating, current ramp-up and ramp-down, deuterium wall-loading and gas puffing, all of which can induce L/H or H/L transitions as appropriate. Also, operating close to critical threshold powers allows the plasma confinement conditions to change gradually (e.g., grassy ELMs to ELM free). We describe some of these here to illustrate the advantage of combining diagnostic systems.

^{a)}Present address: Department of Physics, Imperial College of Science and Technology and Medicine, Prince Consort Road, London, SW7 2BZ, UK.

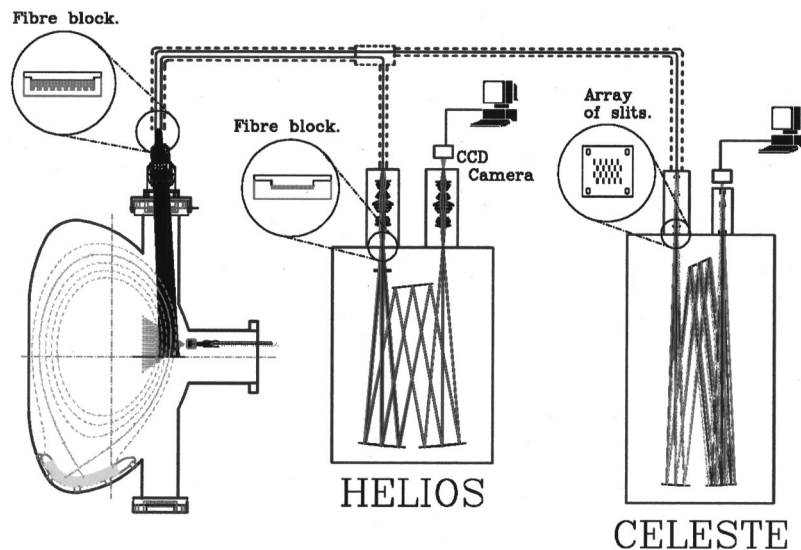


FIG. 1. Schematic arrangement of the combined HELIOS and CELESTE diagnostics including details of the fiber bundle arrangements and spatial localization of helium jet and lines of sight through edge region of COMPASS-D.

A. Spectrometer views

The arrangement of the combined HELIOS and CELESTE diagnostics is shown schematically in Fig. 1.

A collection lens (aperture $f/2$, 100 mm focal length) at an outboard vertical port images the midplane to arrays of fibers bundles. These are routed to the two spectrometers of HELIOS (10 viewing chords) and CELESTE (20 chords). One fiber bundle can be illuminated with a spectral lamp to provide a fiducial line to the high resolution CELESTE spectrometer allowing absolute velocity measurements to be made in the presence of spectrometer drifts. The common optics facilitates absolute sensitivity calibration of all the systems using an integrating sphere enclosing a standard tungsten lamp. For absolute wavelength calibration spectral lamps are used. A collimated jet of helium atoms is provided by a nozzle just above the midplane controlled by a piezo valve. In practice, a steady influx, typically, $\sim 10^{19} \text{ s}^{-1}$, is admitted throughout the discharge. This provides spatial localization for measuring T_e and n_e edge profiles from HeI spectral line ratios.

The localization provided by the helium jet is also put to good use by tuning the CELESTE spectrometer to HeII emission from the resonance line at $\lambda_0 = 468.6 \text{ nm}$ ($n = 3 \rightarrow 4$). The HeII is produced locally from ionization of the thermal helium beam atoms ($\lambda_{\text{ion}}^{0 \rightarrow 1} \approx 3 \text{ mm}$). These ions are further ionized after $\lambda_{\text{ion}}^{1 \rightarrow 2} \approx 3 \text{ m}$ which is smaller than the toroidal circumference $2\pi R \approx 4 \text{ m}$ on COMPASS-D. Hence, the detected HeII emission can also be regarded as localized.

In the case of HELIOS, emission from the helium jet is imaged onto an array of $10 \times 400 \mu\text{m}$ fibers. This gives a spatial resolution of $\sim 5 \text{ mm}$ and a coverage of $\sim 50 \text{ mm}$, encompassing the separatrix as shown schematically in Fig. 1. The CELESTE fiber bundles ($20 \times 2 \times 400 \mu\text{m}$) are immediately adjacent giving 20 chords, with the same spatial coverage as HELIOS in the midplane, but with a superior resolution of $\sim 2.5 \text{ mm}$.

Note the different spectrometer input slit arrangements in the HELIOS and CELESTE spectrometers. The extra fibers used in CELESTE, to improve the photon statistics, can be exploited because slits can be placed side by side at the

spectrometer due to the smaller spectral coverage required for Doppler spectrometry. In a wide spectral coverage spectrometer it is generally not possible to have multiple input slits for multiviewing; instead image dissection of a single slit is generally used.

B. Spectrometry

The design and operation of the spectrometers and associated apparatus have been described in detail in previous publications: T_e and n_e from HeI line ratios (HELIOS),² and T_i , V_ϕ , and V_θ from Doppler spectroscopy (CELESTE).³ Although quite different in their functions, there is much in common with the high resolution CELESTE and the wide spectral coverage HELIOS spectrometer: both use astigmatism-corrected Czerny–Turner configurations, providing good imaging qualities, and so allowing the use of the multiple input slits, or slit dissection, with minimal cross talk. Also, both systems incorporate similar two-dimensional (2D) CCD cameras.⁴ The main features of interest here are summarized in the following sections.

1. HELIOS

Line emission from neutral helium injected at the plasma boundary can provide edge localized measurements of T_e and n_e . Emission from the helium jet is imaged on to an array of fibers as described above. The emerging light from the fibers is imaged at the entrance of an astigmatism-corrected Czerny–Turner spectrometer (Hilger analytical, 0.6 m, $f/4.5$), fitted with $100 \times 100 \text{ mm}^2$, 300 g/mm ruled grating using a pair of camera lenses (50 mm:100 mm) in a front-to-front mount to magnify the image and thus match the f number of the fibers to the spectrometer. At the exit plane a second pair of camera lenses (100 mm:35 mm) demagnifies the focal plane onto a CCD camera⁴ giving a spectral coverage of 125 nm. The Peltier cooled CCD (385×578 , $22 \mu\text{m}^2$ pixels) has a row-shift time of $1 \mu\text{s}$. Vertical binning of the individual 10 spectra is used, with an overall binning time of $300 \mu\text{s}$. Smearing from interchord cross talk

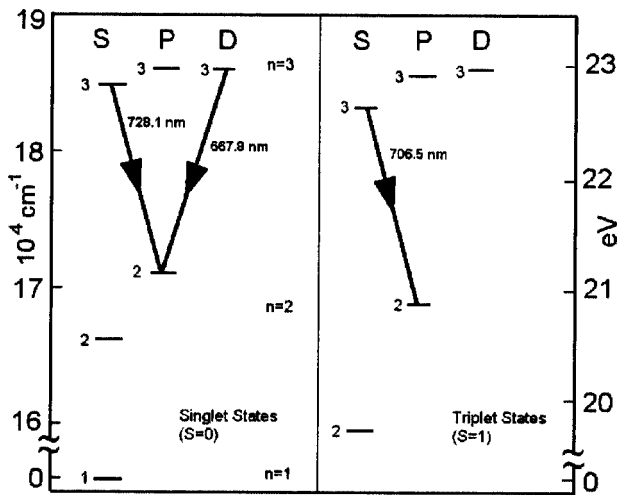


FIG. 2. Term structure of HeI transitions.

arising while the spectra are being clocked down past each other (the present system has no optical gating) is removed numerically.²

The ionization potential of helium (24.6 eV) allows the helium to penetrate a few cm in typical edge conditions ($n_e \lambda_i \sim 10^{17} \text{ m}^{-2}$, for $T_e \geq 30 \text{ eV}$, where λ_i is the $1/e$ penetration depth).

The term-structure relating to the HeI lines used is shown in Fig. 2. The use of both singlet and triplet transitions is the key to obtaining both T_e and n_e estimates from line ratios. This is primarily because the triplet states can only be excited from the singlet state ground state through resonant electron spin exchange with the background electrons whereas the allowed excitations within the singlet, or triplet, configuration are provided by the electron energy continuum above the excitation energy. The effect of the presence of the metastable state $1s2s^3S$ is to introduce a time dependence as the state populations reach equilibrium. This effectively causes some spatial smearing when He atoms traverse the T_e and n_e profiles.

The intensity ratios of the singlet-singlet R1 ($1s2p^1P-1s3p^1D$ and $1s2p^1P-1s3s^1S$ at 667.8 nm and 728.1 nm) and the singlet-triplet R2 ($1s2p^1P-1s3s^1S$ and $1s2p^3P-1s3s^3S$ at 728.1 nm and 706.5 nm) line pairs depend mainly on n_e and T_e , respectively. Excitation from the $1s2s^3S$ triplet metastable state populates the triplet configurations and gives the slowest time dependence in reaching the equilibrium level populations. However, with room temperature helium this is not a major problem, since the relaxation length at 300 K scales as $\sim 5 \times 10^{15} \text{ m}^{-2}/n_e$, giving a radial resolution of $\sim 5 \text{ mm}$ at 10^{18} m^{-3} which matches reasonably well with the optical resolution.

A key requirement in the unfolding of T_e and n_e from spectral-line ratios is that the functional dependence should be as close as possible to orthogonal. In Fig. 3, loci of sample line-ratios R1 (667.8 nm/728.1 nm) and R2 (728.1 nm/706.5) are shown in T_e and n_e space. A particular R1 traces a locus which when intersected by a corresponding locus of R2 defines a unique T_e and n_e . Orthogonal intersections of the loci will provide the least sensitivity to errors and noise. This is clearly satisfied over most of the parameter

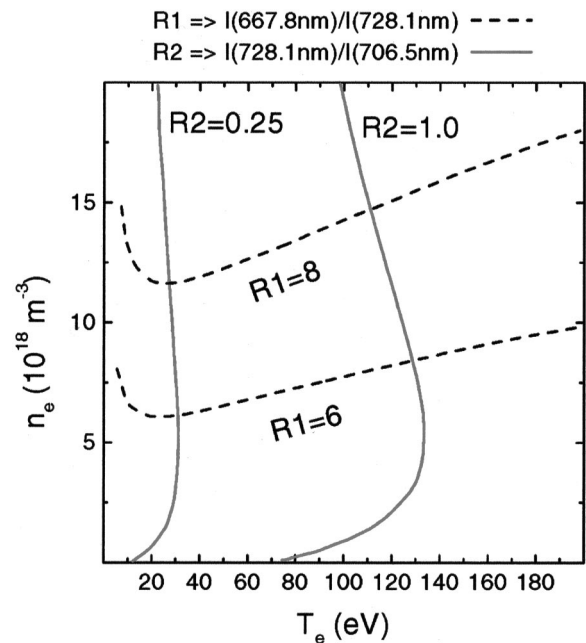


FIG. 3. Calculated dependence of the HeI line ratios on T_e and n_e .

range. The relatively weak line at 728.1 nm can be problematic, emphasizing the importance of measuring the spectrally adjacent background light, as performed in this case by the multichannel CCD detector system, to permit background subtraction.

In the present exercise, the HELIOS spectrometer has also recorded simultaneously the Balmer D_α (and H_α) (656 nm) light along the same viewing chords as the HeI lines. However, the Balmer intensities are not localized like the HeI in the jet, but radiate in ‘onion’ layers requiring unfolding to obtain local emissivities. In the region of interest, it can be reasonably assumed that the emissivity is a flux function, similar to T_e and n_e which are primarily responsible for the ionization and the distribution of excited atomic levels. There is also the implicit assumption that the neutral influx is uniform for the selected region. The chord-integral intensity measurements are inverted to give emissivity as a function of flux surface by the following technique. We characterize the system with a time-dependent set of simultaneous equations described in matrix form as $\vec{I}(t) = \mathbf{A}(t)\vec{\epsilon}(t)$, where $\vec{I}(t)$ is an N -element vector describing the N chord intensities and $\mathbf{A}(t)$ is the $N \times N$ matrix describing the weighting from the flux-surface emissivity vector $\vec{\epsilon}(t)$ to the chordal measurements. An iterative maximum-entropy algorithm is used to give the underlying emissivity distribution by incorporating forward calculation of trial emissivity profiles to intensities, whilst minimizing the fitting χ^2 . This is generally preferable to a matrix-inversion technique which can be unduly affected by uncertainties arising from noise and, in this case, from flux surface geometries. The flux surfaces are obtained from the magnetic diagnostics using the EFIT code.⁵ Absolute emissivity values are obtained from the sensitivity calibration which uses a calibrated integrating sphere and tungsten lamp to illuminate the collection lens so that the whole system is calibrated in one step.

Finally, the neutral density distribution n_D is extracted

HELIOS & CELESTE Data: Shot # 28532

—○— at 0.075 s, —□— at 0.090 s, —▲— at 0.120 s,
 $\Delta r_{\text{slit}} = 0.0$ cm

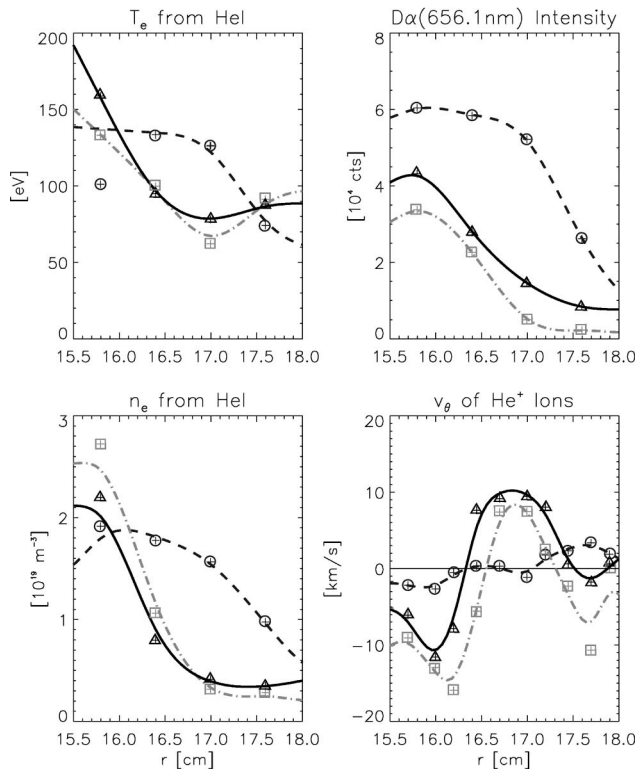


FIG. 4. Changes in profiles of, D_α and V_θ from L-mode, ELMy H-mode and ELM-free H-mode phases.

from the emissivity, electron temperature, and density profiles using a collisional radiative model incorporated in the ADAS⁶ atomic data and simulation code.

2. CELESTE

Light from 20 views of the COMPASS-D plasma illuminates a 4×5 array of slits (typically $400 \mu\text{m}$ wide), laser cut into a metal foil, at the input of the spectrometer preceded by image and aperture optimizing optics to relay the light from the fiber bundles. The foil is mounted on a movable alignment carriage. A Czerny–Turner (Hilger analytical; $f/10$, 1 m focal length) spectrometer is used to disperse the spectrum using a $100 \times 100 \text{ mm}^2$, 2400 g/mm holographic grating. A narrow-band interference filter at the spectrometer exit is used to avoid spectral overlap from slits on the same row.

To image the spectra onto the CCD sensor, an anamorphic lens system is used to change the aspect ratio of the image by ~ 1.5 , using a demagnification of 3 in height and 2 in the spectrum dispersion direction. (The system was also slightly astigmatic to correct the astigmatism of the spectrometer and so reduce the up–down cross talk of the spectral rows.) The unequal demagnification also permits more efficient use of the CCD sensor while maintaining high spectral resolution.

A CCD similar to that on HELIOS is used but with faster row shifting [298×1152 (horizontal \times vertical) active elements, $22.5 \mu\text{m} \times 22.5 \mu\text{m}$, with a $0.3 \mu\text{s}$ row-shift time]. Shared features of the cameras are fluorescent coatings on

the sensors which extend the UV sensitivity to about 200 nm, and Peltier cooling to reduce the dark current and to increase the effective dynamic range. Several rows are illuminated for each spectrum. These are vertically compressed, or binned, into single rows and stored in a shaded region of the chip while a discharge is in progress. This allows for fast spectrum recording (≈ 1 ms).

The spectral response functions, corresponding to each of the slits, are measured with the completely installed system, from the collection lens to the CCD. Narrow emission lines from a spectral lamp (e.g., nickel, mercury and in the present set of experiments from a helium lamp) are used to illuminate the collection lens with a wavelength close to the plasma line of interest. Instrument functions from all the slits are obtained which automatically caters for spectrometer focusing effects and aberrations, for slit profiles including the detailed imaging of the fibers at the slits. These instrument functions are used in unfolding the data in terms of ion temperature and velocity and the line intensities from convolved best fits to the recorded spectra. To track wavelength register drifts in the spectrometer (e.g., from thermal expansion) one of the chords can be illuminated with a standard spectral lamp during the experiments.

Typical accuracies of 10–20% in ion temperature and 1 km s^{-1} in ion velocities with ~ 1 ms time resolution are obtained from the HeII light arising from the jet, or from intrinsic edge impurities such as CIII.

HELIOS & CELESTE Data: Shot # 28532

—○— at 0.075 s, —□— at 0.090 s, —▲— at 0.120 s,
 $\Delta r_{\text{slit}} = 0.0$ cm

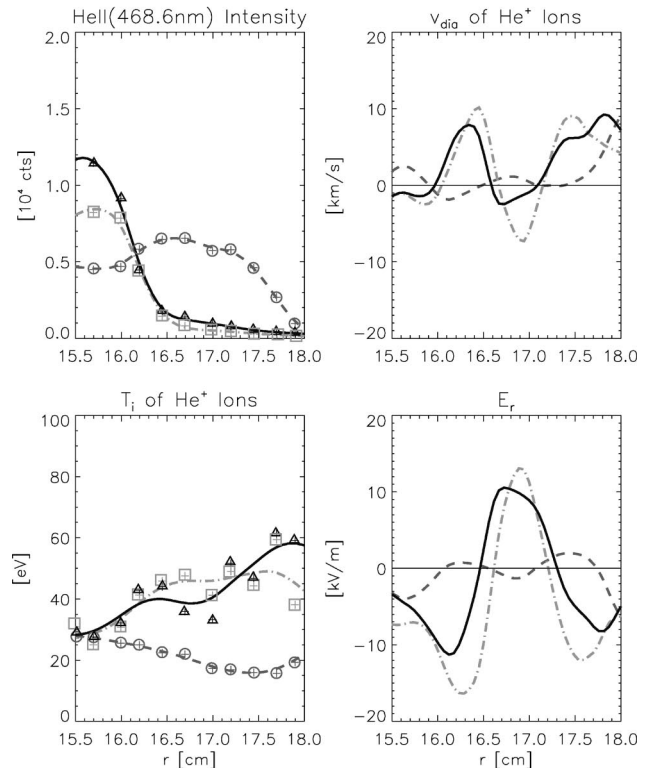


FIG. 5. HeII line intensity (468.6 nm) and T_i , provide the diamagnetic velocity, V_{dia} , obtained from line excitation rates using T_e and n_e (see Fig. 4). The $E_r(r)$, is deduced from radial force balance using V_θ and V_{dia} .

When intrinsic impurity lines are used spatial unfolding is required similar in principle to that for the D_α described above but now including parametrized T_i and V_θ and emissivity profiles, see Refs. 7 and 8 for example.

A near identical CELESTE spectrometer views tangentially in the midplane to monitor the toroidal velocity behavior.

III. RESULTS FROM THE COMBINED DIAGNOSTICS

The synergy arising from intimately combining the three diagnostic systems, HELIOS, CELESTE and the D_α detector array, comes about in both the diagnostics and in the physics investigations. In the former, information from one system is used on another to extract more physical quantities than available independently. Also, cross checking of interpretations of the data are possible. The second stage in the synergy arises in the physics, especially in determining the important parameters governing, for example, the H-mode

transition and evolution and in determining the causality of events. We will deal with these separately drawing on examples of L-mode to H-mode transitions.

A. Diagnostic synergy

Results from a plasma with L- and H-mode phases are shown in Fig. 4. The sample profiles of T_e , n_e , D_α intensity and V_θ during L-mode ($t=0.075$ s), ELMy H-mode ($t=0.120$ s) and ELM-free H-mode ($t=0.090$ s) are obtained independently from the HELIOS and CELESTE diagnostics. Sufficiently strong HeII line emission (468.6 nm) is produced (see Fig. 5) in the region of interest to allow both V_θ and T_i measurements from Doppler effects (Zeeman and Stark splitting are negligible in these conditions).

We can now extract the radial electric field from these sets of measurements. First, for the radial force balance we have for the impurity species $z = \text{HeII}$:

$$\vec{E} = \underbrace{-\vec{v}_z \times \vec{B}}_{\text{Lorentz}} + \underbrace{\frac{\nabla p_z}{Z_z e n_z}}_{\text{dia}} + \underbrace{\frac{m_z (\vec{v}_z \cdot \nabla) \vec{v}_z}{Z_z e}}_{\text{inertia}} + \underbrace{\frac{\nabla \cdot \pi}{Z_z e n_z}}_{\text{visc}} + \underbrace{\frac{\vec{R}_{z0}}{Z_z e n_z}}_{\text{neutral fric}} + \underbrace{\frac{\sum_\beta \vec{R}_{z\beta}}{Z_z e n_z}}_{\text{coulomb fric}}. \quad (1)$$

Only the contribution from the Lorentz force $-\vec{v}_z \times \vec{B}$ and the pressure gradient $\nabla p_z / (Z_z e n_z)$ have to be considered since the other terms, normalized to the pressure gradient term, scale as follows: inertia $\propto M_z^2 \approx 0.04$, perpendicular viscosity $\propto M_z \rho_z / L_\perp \approx 0.07$, neutral friction $\propto M_z L_\perp / \lambda_{zn} \approx 3 \times 10^{-6}$, Coulomb friction $\propto M_z L_\perp / \lambda_{zi} \approx 5 \times 10^{-5}$ where $M_z = v_{z\theta} / v_{zth}$, ρ_z the Larmor radius, L_\perp the typical pressure gradient length, and $\lambda_{\alpha\beta}$ the mean free path for collisions between particle of species α with β . Also the contribution arising from the toroidal velocity v_ϕ can be neglected. This is because on COMPASS-D the toroidal velocity is usually smaller than v_θ (Ref. 9) and being weighted with $B_\theta / B_\phi \approx 0.1$ it is negligible. Therefore, the radial electric field can be reasonably approximated by

$$E_\psi = \frac{\nabla p_z \cdot \vec{e}^\psi}{Z_z e n_z} - v_{z\theta} B_\phi, \quad (2)$$

where the use of the flux-coordinate ψ is discussed in more detail below. The velocity contribution, $v_{z,\text{dia}}$, from the helium ion pressure gradient, ∇p_z , to the observed poloidal velocity, $v_{z\theta}$, remains to be determined. This is obtained from scale lengths and the He⁺ temperature and toroidal magnetic field, i.e.,

$$v_{z,\text{dia}} = -\frac{T_z}{Z_z e B} \left(\frac{1}{L_{n_z}} + \frac{1}{L_{T_z}} \right). \quad (3)$$

The He⁺ temperature scale length, L_{T_z} , is obtained directly from the Doppler measurements. The He⁺ ion density, n_z , is not measured directly but since the line intensity, $I_z = n_e n_z \chi$, where χ is the excitation rate, we can substitute the scale lengths of the I_z , n_e and χ to give

$$v_{z,\text{dia}} = -\frac{T_z}{Z_z e B} \left(\frac{1}{L_{I_z}} + \frac{1}{L_{T_z}} - \frac{1}{L_{n_e}} - \frac{1}{L_\chi} \right). \quad (4)$$

Excitation rate coefficients from ADAS⁶ are used in calculating the χ scale length. Examples of $v_{z,\text{dia}}$ for He⁺ are shown in Fig. 5. These are used in the computation of E_r , also shown in Fig. 5. The similar magnitudes of $v_{z,\text{dia}}$ and directly observed V_θ show the importance of including the former when determining E_r , at least for He ions.

B. Physics synergy

The determination of several plasma parameters in fine spatial detail and with almost perfect mapping now allows us to investigate how these change in controlled experiments. To exemplify the value of diagnostic synergy we now include analysis of the neutral density and use experiments where the edge neutral density was changed periodically during a H-mode discharge by controlling the deuterium gas puffing. Results from these experiments are also used to illustrate the importance of referencing the derived profiles to the coordinate, or dimension, of importance to the physics; in this case, the normalized flux surfaces which we discuss below.

To investigate the evolution of the plasma edge profiles ELM-free H-modes were generated in ohmic SND discharges by shutting off the gas fueling. Within this ELM-free phase a stepped gas puff was applied to trigger a transition back into L-mode followed by a subsequent second L–H transition and another ELM-free phase. Figure 6 shows time traces for the shots Nos. 28443 (red; without gas puff), and

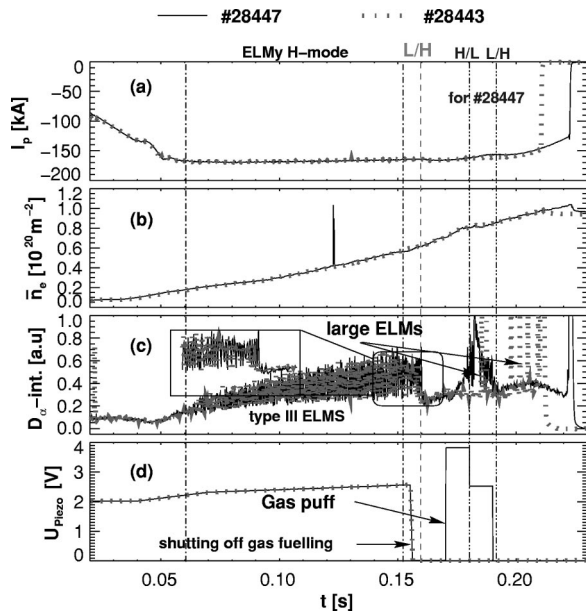


FIG. 6. Waveforms for COMPASS-D shot Nos. 28447 and 28443 showing the effects of gas puffing controlling L- to H-mode transitions.

28447 (black; with gas puff) of (a) plasma current I_p , (b) line averaged density \bar{n}_e , (c) averaged D_α intensity through the X point, and (d) the driving voltage of the piezo valve U_{Piezo} controlling the inlet of deuterium. The sudden drop of the D_α intensity at $t \approx 0.16$ s [trace (b)] indicates the transition to an ELM-free H-mode 3 ms after termination of the gas fuelling. In ohmic discharges on COMPASS-D we usually observe a gradual transition between L-mode and ELM-free H-mode through a “dithering” ELMy phase, and the D_α traces (c) show type III ELMs before the ELM-free phase. In shot No. 28447 a stepped gas puff was applied at $t_3 = 0.18$ s [trace (d)]. The bigger first-part ($\Delta t = 10$ ms) triggers an H–L transition which then is sustained by the slightly smaller second-part ($\Delta t = 10$ ms). After the gas is shut-off the plasma again enters into an ELM-free H-mode.

In the confined region of a tokamak, a number of quantities including n_e , T_e , and \vec{E} may be considered constant to a good approximation on poloidal flux surfaces. However, the flux surface positions change in time, as can be seen from Fig. 7, which shows the evolution of the profile of the nor-

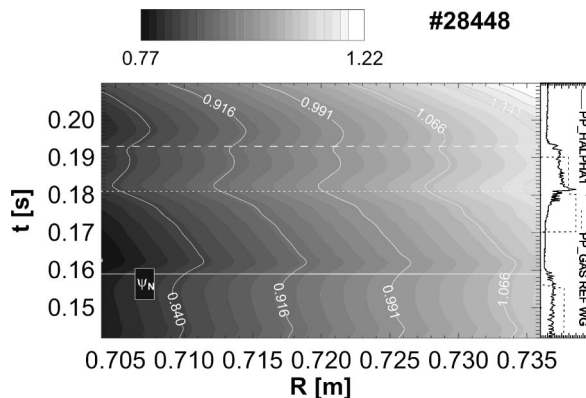


FIG. 7. Evolution of the radial profile of the normalized flux ψ_N in the observed region for shot No. 28448. The horizontal lines mark the transition times as can be seen from the D_α trace (right).

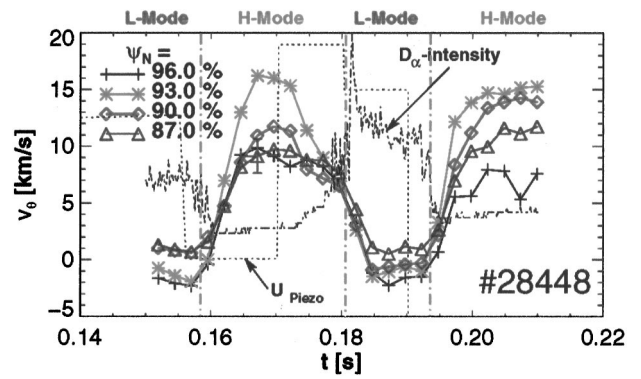


FIG. 8. Poloidal velocity on constant flux surfaces as a function of time.

malized flux function ψ_N within the observed region for shot No. 28448, where $\psi_N = (\psi - \psi_0) / (\psi_S - \psi_0)$ (with ψ_0 and ψ_S denoting the flux on the magnetic axis and the separatrix, respectively). To mark the different phases of the shot traces of the D_α intensity at the midplane and the reference wave-form of gas puff are shown at the right edge.

It is therefore useful to introduce flux coordinates (ψ, θ, ϕ) with $\psi(R, Z; t)$ the poloidal flux function, $\theta(R, Z; t) = \tan^{-1}[(Z - Z_0)/(R - R_0)]$ the usual poloidal angle with $R_0(t)$ and $Z_0(t)$ corresponding to the position of the magnetic axis, and $\phi = -\varphi$ the toroidal angle defined with direction opposite to that for the usual cylindrical machine coordinate system (R, φ, Z) see Ref. 10 for details. The flux coordinate system is then uniquely defined by the unit vectors

$$\vec{e}^\psi = \frac{\nabla \psi}{|\nabla \psi|}, \quad \vec{e}^\theta = \frac{\nabla \theta}{|\nabla \theta|}, \quad \vec{e}^\phi = -\vec{e}^\varphi, \quad (5)$$

following the notation in Ref. 10. Note, that \vec{e}^ψ and \vec{e}^θ are not orthogonal to each other. We use EFIT equilibrium reconstructions⁵ for calculating the unit vectors for each time step. At the midplane this coordinate system, though strictly only defined on closed flux surfaces, can be extended into the scrape off layer (SOL). Figure 8 shows time traces of the poloidal velocity along surfaces of constant normalized flux ψ_N . To illustrate the different phases of the shot the D_α intensity and gas-puff control signal U_{Piezo} are also depicted. Note that the data are plotted at the end of each signal-integration interval to avoid confusion with the causality of events. The most striking feature is that there is no evidence for change in velocity shear prior to the L–H transitions

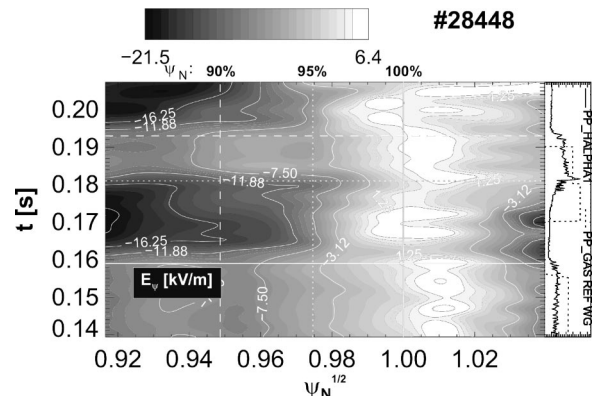


FIG. 9. Evolution of the radial electric field for shot No. 28448.

witl
the

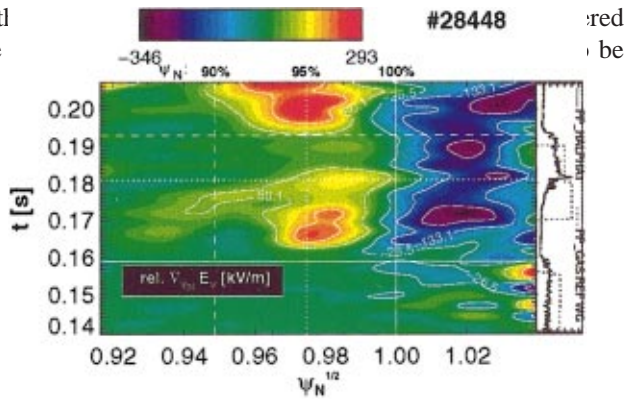


FIG. 10. (Color) Evolution of $dE_\psi/d\psi$ relative to the shear during the first L-mode phase for shot No. 28448.

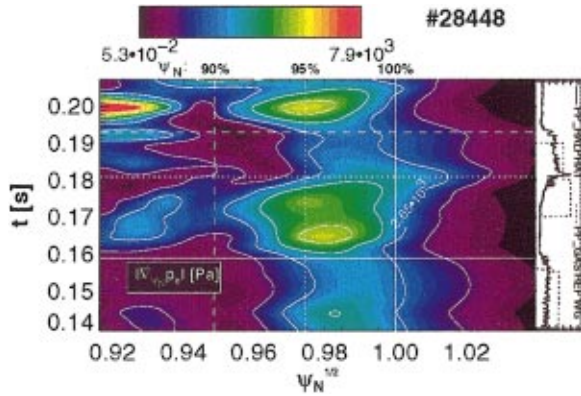


FIG. 11. (Color) Evolution of the electron pressure gradient profile, $dp_{e\psi}/d\psi$, for shot No. 28448.

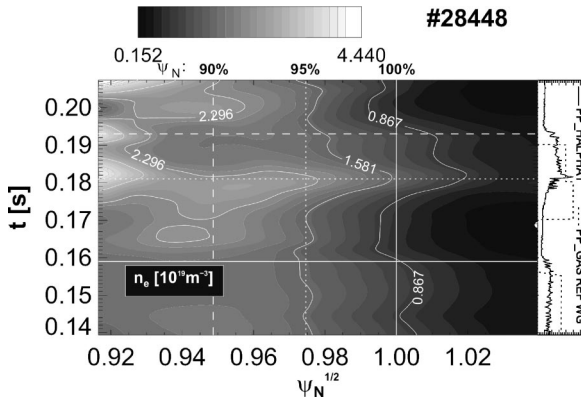


FIG. 12. Evolution of the electron density profile for shot No. 28448.

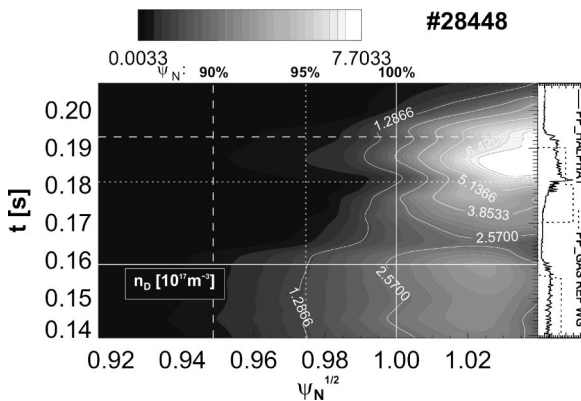


FIG. 13. Evolution of the neutral density profile, n_D , for shot No. 28448.

red
be

seen from Fig. 9 showing E_ψ). However, the HeII velocity can differ substantially from the bulk plasma ion velocity. A more fundamental quantity is the radial electric field $E_\psi = \vec{E} \cdot \nabla \psi / |\nabla \psi|$. In the following we show further contour plots of the evolution of analyzed parameters from shot No. 28448. In Figs. 9–13 the abscissa is $\sqrt{\psi_N} \sim r/a$ and the vertical lines correspond to the 90%, 95%, and 100% (separatrix) flux surfaces as indicated. The horizontal lines mark the transition times as can be seen from the D_α traces at the right edge of the graphs.

The evolution of the electric field E_ψ is shown in Fig. 9. Within the confined region E_ψ points inwards, i.e., is negative, with higher values in the H-mode phase and a maximum change of $\Delta E_\psi \approx -12$ kV/m. The maximum shear in the electric field, $\partial E_\psi / \partial r \approx 2 \times 10^3$ kV/m² is located at \approx the 96% flux surface as can be seen from Fig. 10 showing the change of $\partial E / \partial \psi_N$ with respect to the first L-mode phase. Figures 12 and 13 show the evolution of the electron density, n_e , and the neutral density, n_D . It can be seen that during the L-mode phase the neutral density profile extends further into the plasma than in H-mode.

Therefore, our first attempts at intimately combining disparate diagnostics have yielded new insights into H-mode physics, in particular the role of radial electric field and the formation of a transport barrier during H-mode evolution. Some aspects of the effects of neutrals coming from the SOL have been revealed but further investigations are required to imagine what role, if any, they play in the vicinity of the thermal barrier.

ACKNOWLEDGMENTS

The authors are grateful to M. Brix for providing data for Fig. 3, to C.A. Bunting for diagnostic design, to S.J. Fielding and the COMPASS-D team for running COMPASS-D experiments, and to P. Helander for theoretical guidance. This work was jointly funded by the UK Department of Trade and Industry and EURATOM. H.F.M. is funded by a Marie Curie Research Training Grant.

- ¹J. W. Connor and H. R. Wilson, *Plasma Phys. Controlled Fusion* **42** (2000).
- ²A. R. Field, P. G. Carolan, N. J. Conway, and M. G. O'Mullane, *Rev. Sci. Instrum.* **70**, 355 (1999).
- ³P. G. Carolan *et al.*, *Rev. Sci. Instrum.* **68**, 1015 (1997).
- ⁴Wright Instruments Ltd., Unit 10, 26 Queensway, Enfield, Middlesex, EN3 4SA, UK.
- ⁵L. L. Lao *et al.*, *Nucl. Fusion* **25**, 1611 (1985).
- ⁶H. P. Summers, JET Report No. JET-IR(94)06, 1994.
- ⁷G. Fussman, H. Meyer, and E. Pasch, *Contrib. Plasma Phys.* **36**, 501 (1996).
- ⁸N. J. Conway *et al.*, *Rev. Sci. Instrum.* **70**, 934 (1999).
- ⁹P. G. Carolan *et al.*, *22nd European Physical Society Conference on Controlled Fusion and Plasma Physics* (European Physical Society, Europhysics Letters, 27 Rue de la Vendée, POB 69, CH-1213 Petit Lancy 2, 1995), Vol. 21a, pp. 273–276.
- ¹⁰R. D. Hazeltine and M. J. D., *Frontiers of Physics* (Addison-Wesley, New York, 1992), Vol. 86.